Biomaterials 294 (2023) 122024

Contents lists available at ScienceDirect

Biomaterials

journal homepage: www.elsevier.com/locate/biomaterials

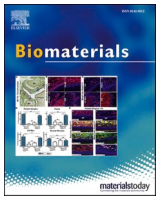

Revealing the complexity of ultra-soft hydrogel re-swelling inside the brain

Michael Shur [a], Outman Akouissi [a,b], Olivier Rizzo [a], Didier J. Colin [c], John M. Kolinski [d], Stéphanie P. Lacour [a,*]

[a] Bertarelli Foundation Chair in Neuroprosthetic Technology, Laboratory for Soft Bioelectronic Interfaces, Neuro-X Institute, École Polytechnique Fedérale de Lausanne (EPFL), 1202, Geneva, Switzerland
[b] Bertarelli Foundation Chair in Translational Neuroengineering, Institute of Bioengineering, Center for Neuroprosthetics, École Polytechnique Fédérale de Lausanne (EPFL), 1202, Geneva, Switzerland
[c] Preclinical Imaging Platform, Faculty of Medicine, University of Geneva, 1211, Geneva, Switzerland
[d] Laboratory of Engineering Mechanics of Soft Interfaces, Institute of Mechanical Engineering, École Polytechnique Fédérale de Lausanne (EPFL), 1015, Lausanne, Switzerland

ARTICLE INFO

Keywords:
Hydrogel
Brain
Radiopaque hydrogel
Implant
Mechanics

ABSTRACT

The brain is an ultra-soft viscoelastic matrix. Sub-kPa hydrogels match the brain's mechanical properties but are challenging to manipulate in an implantable format. We propose a simple fabrication and processing sequence, consisting of de-hydration, patterning, implantation, and re-hydration steps, to deliver brain-like hydrogel implants into the nervous tissue. We monitored in real-time the ultra-soft hydrogel re-swelling kinetics *in vivo* using microcomputed tomography, achieved by embedding gold nanoparticles inside the hydrogel for contrast enhancement. We found that re-swelling *in vivo* strongly depends on the implant geometry and water availability at the hydrogel-tissue interface. Buckling of the implant inside the brain occurs when the soft implant is tethered to the cranium. Finite-element and analytical models reveal how the shank geometry, modulus and anchoring govern *in vivo* buckling. Taken together, these considerations on re-swelling kinetics of hydrogel constructs, implant geometry and soft implant-tissue mechanical interplay can guide the engineering of biomimetic brain implants.

1. Introduction

Implantable neural interfaces are miniaturized devices allowing for direct communication with the nervous system. The brain is an ultra-soft viscoelastic matrix immersed in cerebrospinal fluid that sustains cyclic micromotion induced by breathing and cardiac patterns. The design of neural implants that display biomimetic physio-chemical features of the brain is sought after to improve their long-term bio-integration [1–4]. A "stealth neurotechnology" may therefore have to rely on brain-like viscoelastic materials, ultra-miniaturized layouts, or a combination of the two. Such materials and designs may reduce the micromotion-induced stresses at the tissue-implant interface and alleviate the foreign body reaction (FBR) extent. Recent reports on neural nanomeshes and neural laces promote ultra-thin designs with subcellular footprints to form stable and reliable electrode-neuron interfaces for long-term recordings [5–8]. Their insertion into the brain, however, may be cumbersome, requiring accessories or complex techniques such as liquid injection, robotic assistance or transient scaffolds [9,10]. Mechanically matched and microfabricated implants have been recently demonstrated to reliably interface peripheral nerves [11] and the surface of the central nervous system [12]. However, matching the softness of the brain, with elastic moduli in the sub-kPa range, remains a challenge.

Hydrogels, a class of soft materials, can be engineered to display mechanical properties, high water content and porosity that resemble those of the brain. The palette of polymers and cross-linkers used for the design of hydrogels is vast, including both natural and synthetic polymers, covalent, non-covalent or physical cross-linkers, and allows tuning their mechanical properties even to the softest biological tissue in the body, i.e. the brain [2]. Hydrogels can display Young's moduli in the 0.1–1 kPa range, with 60–95% water content, values in the same order of magnitude as that of grey and white matter [13–15]. To date, hydrogels have been mostly integrated into neural interfaces in the form of an external coating layer applied by dip or spin-coating, casting or printing [16–20]. The typical thickness of hydrogel coatings is of several micrometers, although examples of nanometer-thick coatings have been

* Corresponding author.
E-mail address: stephanie.lacour@epfl.ch (S.P. Lacour).

https://doi.org/10.1016/j.biomaterials.2023.122024
Received 30 August 2022; Received in revised form 12 December 2022; Accepted 20 January 2023
Available online 25 January 2023

reported [19–21]. Recently, all hydrogel-based neural interfaces have been proposed, integrating hydrogel substrate and encapsulation layers and soft conducting traces [22–25] – all prototypes are surface implants. The hydrogels' high-water content, however, raises challenges in terms of electrical insulation, which is mitigated by the introduction of a Parylene or silicone barrier layer.

Delivery of a neural implant into the brain requires mechanical puncturing. The implantation procedure results in inevitable shear stress applied at the implant surface. In the case of hydrated hydrogel coatings, tearing, cracking or delamination from the underlying substrate layer ensue [4,9,26]. As a protective measure, hydrogel coatings are thus typically de-hydrated before implantation, transitioning into a stiff and brittle material able to sustain the shear stresses associated with the delivery method into the biological target. Once *in vivo,* the hydrogel coatings undergo re-swelling, absorbing water from the surrounding tissue and transitioning back to the hydrated state, providing the desired soft interface with the tissue.

Surprisingly, quantitative analysis of *in vivo* recovery of the hydrogel's functional properties following *in vivo* re-swelling has not been reported, and the recovery is often considered to be complete – assuming the hydrogel regains its initial properties [16,17]. Several studies examined the dimensional recovery of de-hydrated hydrogel-coated neural implants using *in vitro* models, such as agarose gel, but these materials do not accurately imitate the physical chemistry, water content, or mechanical properties of neural tissues [18,27,28]. In the general, non-implantable, context of hydrogel research, studies concerning the physical properties of re-swollen hydrogels are either inconclusive or incomplete: reports on polyethylene glycol (PEG) and polyvinyl alcohol (PVA) hydrogels indicate a wide range of behaviours, spanning from the complete recovery of properties to a significant decrease in swelling ratio and shear and compressive moduli. These results vary with the hydrogel de-hydration method, its composition and initial properties [21,29–31].

This study explores whether an implant entirely composed of hydrogel and initially de-hydrated to enable insertion into the brain, would recover its geometry, structural integrity, and mechanical properties *in vivo*, and what the nature of the dynamic interactions between the re-swelling hydrogel and neural tissues is. An experimental framework is proposed, to systematically study the hydrogel re-swelling process and properties recovery across different biologically relevant scenarios, including direct implantation in brain tissue. Polyacrylamide (PAAm) hydrogels are used as a model for ease of tailoring their modulus and swelling ratio [32]; a PAAm formulation can be readily tuned to fabricate brain-like hydrogels with Young's modulus of 1 kPa or lower. The proposed methods can be adapted to other hydrogels. This study includes therefore a systematic comparison of *in vitro*, *ex vivo* and *in vivo* re-swelling scenarios and assesses the various mechanisms involved in the hydrogel re-swelling process. Using computational and analytical models, our observations are rationalized, to then develop guidelines for the design of ultra-soft hydrogel-based neural interfaces.

2. Materials and methods

2.1. Materials

All chemicals were purchased from Sigma-Aldrich unless specified otherwise. Animal experiments were approved by the Veterinary Office of the canton of Geneva, Switzerland, and conducted following all relevant ethical guidelines (Animal license GE/16/320A).

2.2. PAAm hydrogel synthesis

2.2.1. Pristine PAAm hydrogel

Aqueous acrylamide (AAm) solutions (3, 4, 5 and 6% (w/wH_2O)) were prepared by diluting a 40% AAm stock solution. The cross-linker, N,N' methylenebis (acrylamide) (0.1% (w/wAAm)), and thermo-initiator, potassium persulfate (0.1% w/w), were added and the solution was stirred and then purged with nitrogen in an ice bath for 30 min. Then, the catalyst tetramethylethylenediamine (0.1% v/v) was finally added.

The solution was poured into a mold and sealed with a paraffin film to allow polymerization and curing for 2 h at room temperature (RT). The cured hydrogel was demolded and placed in a de-ionized water (DIW) bath to allow the extraction of any unreacted reagents and to reach equilibrium swelling overnight (ON).

2.2.2. Radiopaque PAAm (rPAAm) hydrogel synthesis

Aqueous AAm solutions (3, 4% (w/wH_2O)) were prepared by diluting a 40% AAm stock solution. Two cross-linkers, N,N′-methylenebisacrylamide (0.07% (w/wAAm)) and N,N′-bis(acryloyl)cystamine (BAC, 0.03% (w/wAAm) in 0.5 mL methanol, Thermo Fisher Scientific)) and the thermo-initiator potassium persulfate (0.1% w/w) were added and the solution was stirred and then purged with nitrogen in an ice bath for 30 min. Then, the catalyst tetramethylethylenediamine (0.1% v/v) was finally added and the solution was poured into a mold and sealed with paraffin film to allow polymerization and curing. The cured hydrogel was de-molded and soaked in $KAuCl_4$ aqueous solution (20 mL, 0.1 mM) for 30 min and then transferred into $NaBH_4$ solution (30 mL, 0.05 mM) and allowed to soak for additional 15 min. The formation of Au NPs was monitored by the color change of the hydrogel from yellow to dark red. The Au NPs – containing hydrogel was finally soaked in a DIW bath for 24 h to allow the removal of excess reagents and unbound Au NPs, as well as to reach equilibrium swelling.

2.3. Hydrogel shank fabrication

Swollen to equilibrium hydrogel samples were de-hydrated by performing an anisotropic drying process. Disc-shaped samples were placed on a polyethylene terephthalate (PET) sheet and secured to the sheet around their perimeter using an adhesive tape. The tape was used to constrain the shrinkage, resulting from the de-hydration, predominantly to the perpendicular axis and prevent curling and other deformations associated with stresses during water evaporation. Following de-hydration for several days at RT, a thin, uniform, dry hydrogel film was obtained. A final drying step was performed at 80 °C by clamping the dry hydrogel film between two perforated glass plates. Thermal drying was preferred against freeze drying to preserve the hydrogel shank structure. The dry hydrogel film was then machined to the desired shank geometry (3 mm length, 750 μm width) using a femtosecond excimer laser (WS Turret, Optec Laser Systems).

2.4. Mechanical characterization

All measurements were performed at 25 °C using a rheometer (MCR 302, Anton-Paar) equipped with a Peltier heating system and a plate-plate geometry (25 mm plate, sand-blasted). Shear storage modulus was measured in oscillation mode for 60 s (0.5% strain, 1 Hz oscillation frequency). 5 samples were used for each measurement.

2.5. Morphological analysis

Scanning electron microscopy (SEM) images were acquired in high vacuum mode without any additional coating (SU5000, Hitachi). Hydrogel samples were lyophilized prior imaging and then fractured to gain access to bulk morphology.

2.6. Radiopaque PAAm (rPAAm) hydrogel characterization

The loading of the Au NPs inside the hydrogel matrix was evaluated through thermogravimetric analysis. A lyophilized rPAAm sample was heated from 30 to 900 °C in air (10 °C/min heating rate) and the weight residue following the combustion of the organic components,

representing the Au mass, was recorded (TGA 4000, PerkinElmer). The calculated weight percentage of the Au inside the matrix neglected any residual water in the sample, which evaporated before reaching 100 °C. The measurement was repeated for 3 samples.

The Au NPs size was characterized by transmission electron microscopy (TEM). Au NPs were extracted from a fully swollen rPAAm sample by vigorous ultra-sonication in DIW. The pink dispersion was then centrifuged at 4′000 rpm for 5 min and the collected Au NPs were re-dispersed in 2 mL of DIW and filtered through 0.22 μm PTFE filter. TEM samples were prepared by placing a drop of Au NPs dispersion on a glass substrate and then transferring it onto a glow discharge-treated mesh copper grid with a carbon support film. Imaging was performed using a Talos L120C G2 TEM (Thermo Scientific).

To study the long-term stability of the rPAAm in aqueous medium, a sample was soaked for 9 months in DIW. Then, the sample was discarded, and the extraction medium was filtered through 0.22 μm PTFE filter and scanned using a UV–Vis spectrophotometer to detect any characteristic absorption of potentially leached Au NPs. Scans were performed in the visible range (Lambda 365, PerkinElmer). A reference Au NPs dispersion in DIW, prepared by vigorous ultra-sonication of rPAAm and extraction of Au NPs, was used as a reference.

2.7. Initial swelling tests

Fully swollen hydrogel samples were gently blotted with a cotton wipe and their weight was recorded (W_s). Then, the samples were dried at 100 °C under vacuum and weighted again (W_d). The swelling ratio was calculated using the following equation:

$$\%\ \text{swelling} = 1\,00 \times (w_s - w_d) / w_d \tag{1}$$

A minimum of 10 samples were analyzed for each formulation.

2.8. Free re-swelling tests

Fully de-hydrated hydrogel samples were weighted (W_d) and allowed to re-swell in a solvent bath containing either DIW, phosphate buffered saline (PBS) or artificial cerebrospinal fluid (aCSF, Bio-Techne AG). Re-swelling curves were constructed by acquiring a weight measurement of the re-swelling sample at different time points ($W_{rs,t}$). The re-swelling ratio was calculated using equation (1) considering $W_{rs,t}$ and W_d. A minimum of 10 samples were analyzed for each formulation.

2.9. Tissue-assisted ex vivo re-swelling tests

Rat brain was dissected from an adult Lewis rat without performing perfusion. The tissue was kept in PBS at 4 °C and was used within 24 h following the dissection.

Fully de-hydrated hydrogel shanks were first weighted (W_d) and then allowed to re-swell by inserting them into the dissected brain while keeping it in a sealed and humid container at RT. Shanks were removed from the brain at different time points by gently pulling them with tweezers and their weight was recorded ($W_{rs,t}$). The re-swelling ratio was calculated using equation (1) considering $W_{rs,t}$ and W_d.

A minimum of 5 samples were measured for each formulation.

A similar procedure was used to perform *ex vivo* re-swelling experiments with higher water availability. In this case, however, the brain with the inserted shanks was kept immersed in aCSF at RT for 24 h.

2.10. Micro-CT scans

All scans were performed at the "Small animal preclinical imaging platform" (Plateforme d'Imagerie Préclinique du Petit Animal, PIPPA) of the Faculty of Medicine, University of Geneva. Micro-CT scans were performed using a Quantum GX micro-CT scanner (PerkinElmer) at 90 kV acceleration voltage and 88 μA current. Scan parameters were set to 10 mm field of view (FOV) and 20 μm voxel size using the high-resolution preset mode, resulting in a scan time of 14 min. A validation scan in air was performed by placing a rPAAm shank inside an Eppendorf tube. A validation scan in agarose gel was next performed by inserting de-hydrated rPAAm shank (3% AAm) and a reference PAAm shank (3% AAm) into a 3% agarose gel phantom.

Ex vivo scans were performed using a freshly dissected brain of an adult Lewis rat. After dissection, the brain was kept in PBS at 4 °C. Before the scans, the brain was lightly blotted and placed in a plastic holder to fit the scanner. rPAAm shanks of different compositions (3 and 4% AAm) and thicknesses (h_d = 50 and 100 μm) were manually inserted into the brain and the "head" of the shank was cut. The brain was scanned at different time points and was kept in a humid container at room temperature between scans to minimize drying.

For *in vivo* scans, 4 adult female Lewis rats (220 g body weight) were anaesthetized with isoflurane (2–4%) and head-fixed in a stereotaxic frame (David Kopf Instruments). Two craniotomies of approximately 2 mm^2 were performed above each hemisphere and the dura mater was removed. Then, a de-hydrated rPAAm shank (3% AAm, h_d = 50 and 100 μm) was inserted into each hemisphere and the "head" of the shank was cut. The craniotomy was immediately sealed with a room temperature curing tissue silicone sealant (Kwik-Sil, World Precision Instruments) followed by a layer of dental cement and the skin above the skull was sutured. Buprenorphine analgesic (0.1 mL) was subcutaneously administered post-operatively and for the entire duration of the experiment, twice a day.

The animals were scanned at several time points under isoflurane anesthesia.

Three-dimensional image reconstruction was performed using OsiriX software (Pixmeo). At each time point the re-swollen hydrogel shank thickness and width were measured ($h_{rs,t}$, $b_{rs,t}$). The one-dimensional re-swelling was calculated using the following equations:

$$\begin{aligned} h\_re - swelling(t) &= h_{rs,t}/h_d \ ; \\ b\_re - swelling(t) &= b_{rs,t}/b_d \end{aligned} \tag{2}$$

In addition, the cross-section (CS_t) area was calculated at each time point by multiplying the thickness ($h_{rs,t}$) by the width ($b_{rs,t}$). The cross-section increase factor was calculated as follows:

$$CS\_if(t) = CS_t/CS_d \tag{3}$$

A minimum of 3 shanks were used for each formulation/thickness combination.

2.11. In vitro shank buckling validation

Testing of buckling at different re-swelling scenarios *in vitro* was performed by inserting rPAAm shanks (3% AAm, h_d=100 μm) into 3% agarose gel and cutting off the "head" of the shank. In the constrained scenario, a drop of cyanoacrylate adhesive was applied at the insertion point of the shank and a round glass cover slip was placed on top. Photos of the re-swelling shank were taken at different time points.

2.12. Finite element simulation of buckling

The finite-element model was developed and implemented using COMSOL 5.4 software with the structural mechanics module. The calculations use linear elasticity for the material's constitutive response. A stationary study, complemented with a buckling analysis, was chosen for the simulation. The shank consisted of a rectangular part (4 mm × 200 μm) merged with a semicircle with the same thickness, simulating a rounded tip. The shank's properties were represented by an incompressible (implemented through the pressure-based mixed formulation) linearly elastic material with Young's modulus of 1 kPa and Poisson's ratio of 0.49. The top surface of the shank was fully constrained. The elastic response of the brain was modelled by implementing a spring boundary condition (k = 0.1 N/m) [47] on all other external boundaries.

To initiate the buckling process, an initial isotropic volumetric stress was applied to the shank's bulk; the initial stress represents the volumetric expansion during the dry-to-swollen transition due to water uptake after implantation. All plots amplify deformation by a factor of 6 for visualization purposes.

Different studies were then performed by varying the thickness (100, 200, 300 μm), length (3, 4, 5 mm) and Young's modulus (0.5, 1, 2 kPa) of the shank. For all simulations, the first buckling mode was taken into consideration for further analysis.

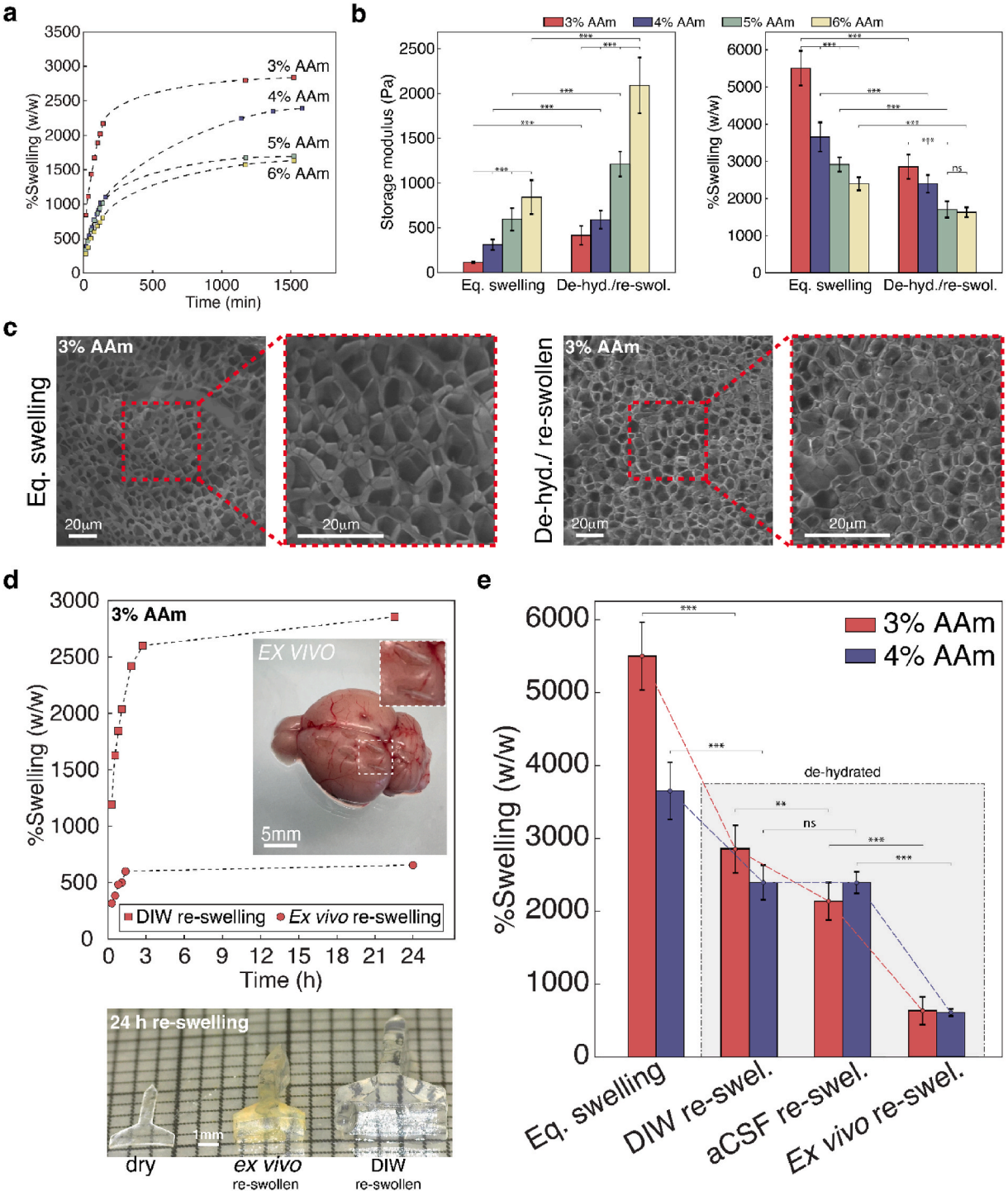

Fig. 1. PAAm hydrogel re-swelling. a) Re-swelling curves of de-hydrated PAAm samples of various monomer concentrations. b) Comparison of the storage modulus (left) and the swelling ratio (right) of different PAAm formulations in the as-prepared equilibrium swelling state and following one cycle of de-hydration/re-swelling in DIW (N = 5–15). c) Morphological comparison of 3% AAm hydrogel samples in the as-prepared equilibrium swelling state and following one cycle of de-hydration/re-swelling in DIW. d) Re-swelling curves of de-hydrated 3% AAm hydrogel shanks using DIW and an explanted rat brain as water source. Initial dry shank geometry: 750 μm width, 100 μm thickness, 3 mm length. e) Comparison of the swelling ratio of 3 and 4% AAm formulations following various re-swelling scenarios (N = 5–15). * denotes $p < 0.05$, ** denotes $p < 0.01$ and *** denotes $p < 0.001$.

2.13. Statistical analysis

All results were reported as mean ± standard deviation unless otherwise noted. One-way analyses of variance (ANOVA) were performed followed by post-hoc Tukey comparison. The significance level was set to $p < 0.05$.

3. Results

3.1. Re-swelling of PAAm hydrogel

3.1.1. Re-swelling of bulk hydrogel in vitro

We designed PAAm gels with a range of stiffness by varying the acrylamide (AAm) monomer concentration from 3 to 6% while keeping the cross-linker concentration constant. PAAm samples were swollen to equilibrium and their storage modulus and swelling ratio were measured (the loss modulus was also recorded but found negligible in our experimental conditions). Storage modulus provides a good estimation of the Young's modulus by using the Poisson's ratio, widely characterized for PAAm hydrogels [33,34]. The softest composition, based on 3% AAm, showed a storage modulus of 115 Pa and a swelling ratio of 5′500% while the stiffest composition (6% AAm) had a storage modulus of 850 Pa and a swelling ratio of 2′400%. First, we studied the hydrogels' recovery in a free re-swelling scenario, in water, thereby eliminating any chemical, thermodynamic or mechanical constraints that might influence the re-swelling outcome. Hydrogel samples were completely de-hydrated and allowed to re-swell in a de-ionized water (DIW) bath until equilibrium was reached, and their storage modulus and swelling ratio were measured again (Fig. 1 a-b). Interestingly, the recovery rates of both the modulus and the swelling ratio were found to depend on the hydrogel composition and initial properties. While the storage modulus of the stiffest 6% AAm composition increased by 2.5 times from 850 to 2′100 Pa and its swelling ratio decreased by 30% from 2′400 to 1′700%, the softest 3% AAm formulation's storage modulus increased by almost 4 times (from 115 to 420 Pa) and its swelling ratio decreased by half (from 5′500 to 2′800%). Intermediate monomer formulations followed the same trend. In parallel, we observed a decrease in the pore size following the de-hydration/re-swelling cycle, as well as partial collapse of the porous network. For example, the average pore size of the softest 3% AAm composition decreased from 6 to 3 μm and some pores were closed or collapsed (Fig. 1c). One must keep in mind that the observed pores are likely to be larger than the actual ones found in the hydrated state because of water crystals formation during the quenching step of the SEM sample preparation. Nevertheless, these pore size measurements can still be used in a comparative manner to highlight eventual morphological changes [35–37]. The latter are an expected consequence of the de-hydration process; as water vanishes, the entire porous network collapses, causing the formation of secondary cross-linking points. Upon re-introducing water into the polymeric network, some of the newly formed inter-chain bonds cannot be broken, thus limiting the subsequent absorption of water and swelling outcome and leading to an incomplete recovery of the hydrogel's properties. In order to account for any possible thermodynamic effects that might limit the diffusion of water into the highly polar PAAm network, we conducted similar re-swelling experiments in physiologically relevant ionic environments e.g. phosphate buffered saline (PBS) and artificial cerebrospinal fluid (aCSF, 3 and 4% AAm only). The osmotic pressure inside charged or highly polar gels is known to depend on the ionic strength of the solvent (Donnan's effect) and to contribute to the gel's swelling behavior [38]. However, little (<30%) to no significant differences were identified when comparing PAAm samples re-swollen in PBS and aCSF, with those re-swollen in DIW (Fig. S1). This might be explained by the relatively low ion concentrations in both solutions (for example, [NaCl] = 137 mM and 119 mM for PBS and aCSF, respectively). The swelling increase associated with Donnan's effect for PAAm has been shown to be non-significant at NaCl concentrations below 250 mM [39].

3.1.2. Re-swelling of micromachined hydrogel shanks ex vivo

Next, we examined re-swelling of the ultra-soft de-hydrated PAAm *ex vivo*. PAAm hydrogel was first de-hydrated in a constrained and anisotropic manner to form a thin, smooth, and uniform dry hydrogel film. Next, we laser-cut the dry PAAm films into pointed shanks with the geometry typical of an intracortical implant. Shanks with the following dry geometries were tested: 50 or 100 μm thickness (*h*), 750 μm width (*b*), and 3 mm length (*l*). Several shanks were manually inserted into freshly explanted rat brain tissue and subsequently removed at different time points during the re-swelling process (Fig. 1d). Free re-swelling measurements of PAAm shanks in DIW were performed in parallel for comparison. Surprisingly, tissue-assisted re-swelling of the shanks resulted in a dramatic decrease in the swelling ratio of the hydrogel, which in the case of the 3% AAm composition decreased from 2′800% in DIW to only 600% when re-swollen *ex vivo*. Visual inspection of the shanks after 24 h re-swelling clearly revealed the reduced swelling of those shanks inserted into the explanted tissue (Fig. 1d). Re-swelling curves indicate that in both re-swelling scenarios the hydrogel shanks reached an equilibrium after 24 h exposure to the re-swelling medium. Fig. 1e summarizes the dramatic reduction of re-swelling recovery of PAAm hydrogel when using the brain as a source of solvent. Compared to the initial swelling capacity of the as-prepared and swollen to equilibrium hydrogel, the swelling capacity of the same hydrogel once it undergoes a de-hydration cycle and is inserted into brain tissue decreases by almost 90% (from 5′500–600%, for 3% AAm). Additional consequences of the decreased swelling ratio of the *ex vivo* re-swollen hydrogel shanks include the corresponding increased stiffness and alternations to the shank size and geometry.

3.2. Realtime visualization of hydrogel re-swelling using micro-computed tomography

3.2.1. Radiopaque PAAm hydrogel

Although explanted brain tissue better mimics *in vivo* conditions compared to a saline solution, it fails to fully reproduce important physiological parameters of the living brain, such as osmotic pressure, CSF re-constitution mechanisms and mechanical characteristics. Furthermore, the water content inside an explanted brain drops over time because of evaporation, which may eventually constrain hydrogel re-swelling due to lower amount of available solvent [40]. Therefore, we developed an experimental approach to quantify the real-time re-swelling recovery of the de-hydrated hydrogel shanks *in vivo*. Inspired by the synthetic approach introduced by Wang et al., we designed a radiopaque PAAm (rPAAm) hydrogel, which has an intrinsic contrast for X-Ray and Computed Tomography (CT) imaging due to *in situ*-formed gold nano-particles (Au NPs) [41] (Fig. 2a). Au NPs are often used as exogenous contrast agents for CT imaging due to their high X-ray attenuation and ease of surface modification, allowing for their covalent bonding to various therapeutic and biological targets [42,43]. The size distribution of the *in situ*-synthesized Au NPs was found to be in the 4–10 nm range, while their loading inside the PAAm matrix was 7.3 wt% of the solid content (Fig. S2). An important feature of the rPAAm relies on the covalent attachment of the Au NPs to the PAAm network, thus preventing their leaching out from the hydrogel matrix (Fig. 2a). Even after soaking the rPAAm in water for 9 months, no traces of Au NPs in the extracting medium could be detected (Fig. S3). The functional properties of the rPAAm, such as its re-swelling kinetics, swelling ratio and storage modulus were compared to standard PAAm in order to identify any potential effects of the disulfide cross-linker or Au NPs. Only a slight decrease in swelling ratio of the rPAAm formulations in comparison to the PAAm formulations was observed, as well as a limited increase in storage modulus. Even after the synthetic modifications of the hydrogel its modulus remained below 1 kPa, ensuring that the rPAAm formulation is still within the physiological range of elastic moduli for brain tissue (Fig. S4).

De-hydrated rPAAm shanks were first used to examine the contrast

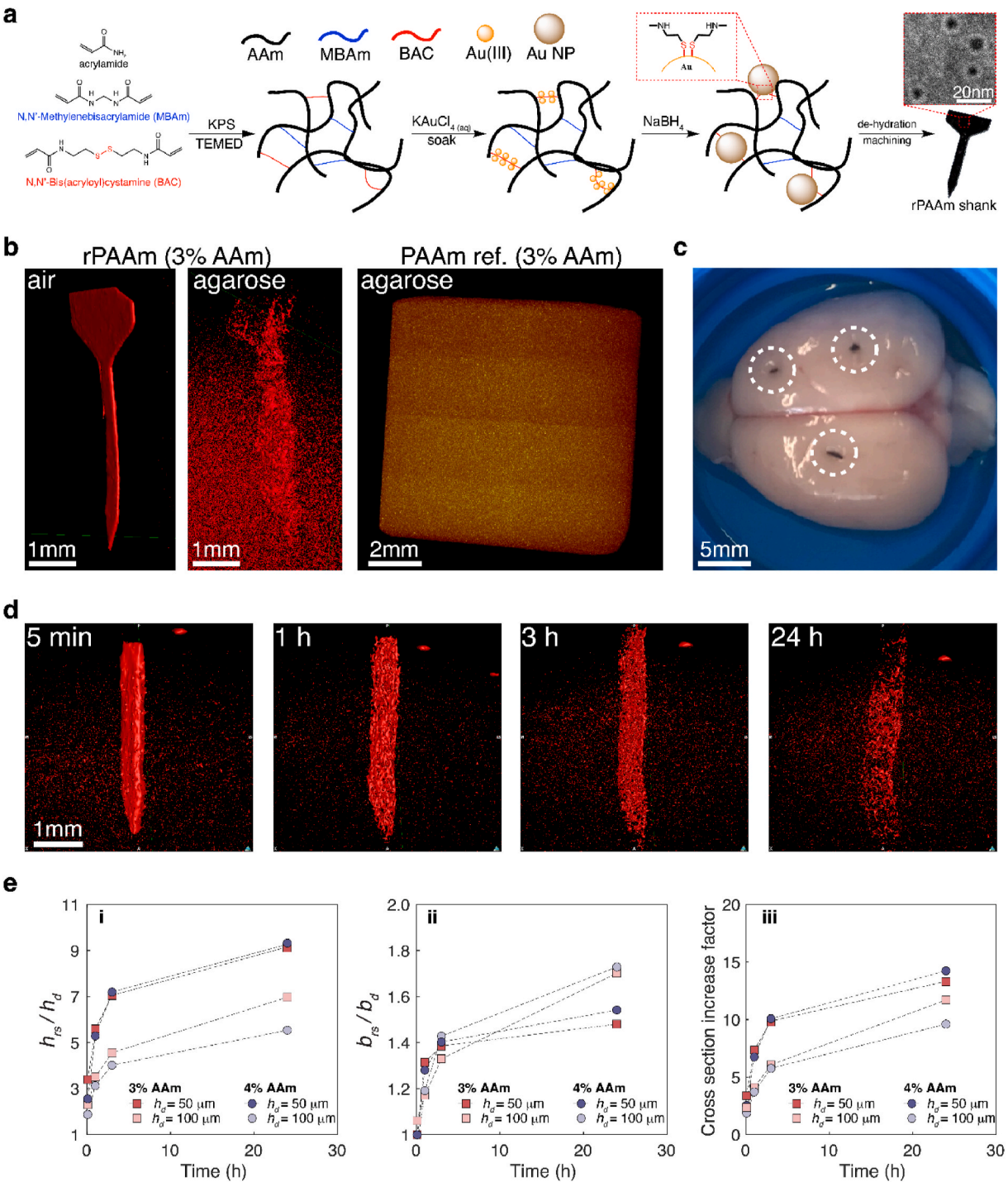

Fig. 2. Radiopaque PAAm (rPAAm) synthesis and re-swelling. a) Synthetic approach for the fabrication of rPAAm hydrogel shanks. b) Contrast validation of rPAAm using agarose gel mockup. c) *Ex vivo* setup for re-swelling study of rPAAm using an explanted rat brain. d). Micro-CT-based 3-D reconstruction at different time points of rPAAm shanks following *ex vivo* re-swelling. e) *Ex vivo* 1-D re-swelling curves of rPAAm shanks of different thicknesses and compositions. Thickness (*i*), width (*ii*) and cross-section (*iii*) increase curves.

and resolution of images acquired using a micro-CT scanner. Validation scans were performed in air and inside an agarose gel phantom. A standard de-hydrated PAAm shank was scanned in parallel as a reference in order to evaluate the contrast enhancement. While the rPAAm shank could be clearly visualized inside the agarose gel due to the contrast provided by the Au NPs, the reference PAAm shank could not be detected (Fig. 2b). We next performed a series of *ex vivo* scans to validate the efficiency of the method to track the re-swelling process in a tissue with sufficient spatial resolution. De-hydrated rPAAm shanks of 2 different thicknesses, 50 and 100 μm, and 2 compositions, 3 and 4% AAm, were inserted into freshly explanted rat brain, and the tissue was scanned at different time points and up to 24 h following the insertion (Fig. 2c). Between the scans, the brain was kept in a sealed, humid container to minimize tissue drying. At each time point a 3-dimensional reconstruction of the shanks was performed, followed by extraction of their geometrical dimensions (Fig. 2d). Re-swelling of the shanks was clearly visible, characterized by an increase of the shanks' thickness (*h*), width (*b*) and length (*l*) between each scan. Water absorption by the

hydrogel shank resulted in reduction of the Au NPs' volumetric concentration, which led to a decrease in contrast, as can be clearly seen in scans performed at longer time points (3 and 24 h). One-dimensional re-swelling curves were constructed by calculating the relative increase in the shanks' thickness and width (Fig. 2e–i-ii). Because of the anisotropic de-hydration procedure, the thickness dimension governed the re-swelling process with a 9-fold increase after 24 h, as opposed to a mild increase of up to 1.8 times in width. To eliminate any possible variations between batches arising from the anisotropic de-hydration procedure, the relative increase of the shanks' cross-section was also calculated (Fig. 2e–iii). In addition, the sensitivity of the micro-CT scans was sufficient to clearly distinguish between shanks of different initial thicknesses, as can be seen in the re-swelling curves.

No significant difference was observed between the 3 and 4% AAm shanks, in agreement with the mass re-swelling results obtained in the *ex vivo* experiments. This contrasts with the free re-swelling experiments in DIW that resulted in a higher re-swelling ratio of the 3% AAm formulation (Fig. 1b). In addition, the micro-CT scans clearly show a size-dependent re-swelling outcome. For both compositions, the thinner shanks were found to re-swell more compared to the thicker ones. This dependence is clearly visible when analyzing the relative thickness increase throughout the re-swelling sequence, as the 50 μm-thick shanks increased their thickness up to twice as much compared to the 100 μm-thick shanks. The difference between the relative width increase of these shank geometries is less pronounced than the relative thickness increase, although still clearly identifiable. The overall "growth" of the shanks' cross-section is therefore mostly governed by the thickness change. The dependence of the hydrogels' re-swelling outcome on its initial dimensions could have important consequences for the performance and reliability of subsequent hydrogel-based neural interfaces because both the functional properties and final dimensions depend on the de-hydrated mass and geometry.

3.2.2. *Re-swelling of radiopaque PAAm shanks in vivo*

Next, we performed an *in vivo* re-swelling study using a rat model. The surgical approach consisted of performing 2 small craniotomies and durotomies over the rat's cortex. Two de-hydrated rPAAm shanks (3% AAm) of varying thicknesses (50 and 100 μm) were manually implanted, one shank in each craniotomy. Following implantation, the "head" portion of the shank, which is used for handling purposes, was removed. The exposed brain was finally sealed using a surgical silicone sealant material (Kwik-Sil) followed by dental cement for mechanical protection. Animals were scanned under anesthesia at different time points and up to 48 h post-implantation, and the micro-CT scans of the shank geometry were reconstructed in order to allow extraction of their geometrical parameters (Fig. 3a and b). Fig. 3c shows two-dimensional coronal slices of the reconstructed images collected from the same animal over 6 time points. Both shanks are visible on each slice, and the thickness increase upon re-swelling is readily apparent from the images. Compared to the *ex vivo* scans, a lower contrast of the shanks was achieved due to the X-ray attenuation by the skull (Fig. S5). Surprisingly, in addition to swelling, buckling of the shanks was observed. While the shanks were perfectly linear upon implantation, they deformed into a tortuous geometry, twisting about the insertion axis. The buckled geometry was found to evolve and amplify with time, both in terms of the twists' amount as well as their amplitude (Fig. 3c). Relative dimensional changes, which are indicative of the re-swelling process, were calculated in a manner like that of the *ex vivo* experiment described above (Fig. 3d–i-iii). Once again, the thinner shanks reached a higher degree of re-swelling, as indicated by their higher relative increase in thickness and cross-section compared to the thicker ones. Interestingly, thin shanks reached a final re-swelling similar to that observed in DIW, corresponding to about 15 times increase of the cross-section, as opposed to only 11 times increase detected for the thicker 100 μm-thick shanks. The shanks' cross-section increased more *in vivo* compared to the *ex vivo* experiment (15-fold *in vivo* vs. 12-fold *ex vivo*), which is likely a consequence of the higher water content and enhanced solvent transport inside the living tissue (Fig. 3d–iii). Quantitative analysis of the shanks' *in vivo* re-swelling was used to determine the time required to reach equilibrium. One animal was scanned 48 h post-implantation and the implanted shanks exhibited some residual swelling as demonstrated by further increase of their dimensions compared to the 24 h scan (Fig. S6), suggesting that shanks implanted in a living tissue require more time to reach equilibrium.

Because CSF regenerates *in vivo*, one can assume that over long timescales, additional solvent becomes available to the gel via diffusion through the brain tissue [44,45]. However, other physiological consequences of water depletion inside the tissue in the vicinity of the hydrogel implants (caused by the water uptake of the re-swelling hydrogel) should be taken into consideration, in particular, the hyperosmotic stress exerted on the neighboring cells. As the solvent absorption by the hydrogel results in changes to the osmolarity of the extra-cellular medium, water flux out of the cells might cause the cells to shrink, which could eventually promote cell de-hydration and apoptosis [44–46]. Hence, cell viability and histological analysis of the tissue surrounding a given hydrogel implant should be performed, in addition to the re-swelling quantification demonstrated here, to examine the extent of the hyperosmotic stress consequences. In fact, the two phenomena might be causing the reverse effects as higher swelling recovery of a given hydrogel implant might also lead to more significant water depletion and the associated hyperosmotic stress, thus leading to severe tissue loss, inflammatory response and degradation in performance or stability of the neural interface.

Further *ex vivo* re-swelling experiments illuminated the importance of water availability inside the tissue for the hydrogel re-swelling outcome. By inserting 100 μm-thick de-hydrated rPAAm shanks (3 and 4% AAm) into two freshly explanted rat brains for 24 h and immersing one of them into aCSF while keeping the other inside a sealed container, a significantly higher swelling ratio was measured for the shanks inside the first brain, independently of AAm concentration (Fig. 3e). In the aCSF immersed sample, unlimited water is available to the inserted shank both via diffusion through the tissue and through the lesion caused upon the shank's insertion into the brain. Both mechanisms contribute to the enhanced re-swelling, as is clearly seen in the re-swelling results. A set of thinner, 50 μm-thick shanks, reached the same swelling ratio in both cases. This observation suggests that the higher water amount required by thicker or larger shanks depletes the tissue locally, whereas the lesser water demand of smaller shanks does not cause similar depletion. The local depletion of water may also account for the slower re-swelling kinetics observed for the thicker shanks *in vivo*, as more water must diffuse towards the shank through the tissue for it to reach equilibrium. Inevitably, the lower solvent gradients in the thicker shank case will result in a slower approach to equilibrium and a longer re-swelling process.

3.3. *In vivo buckling and 2D finite-element modelling of a hydrogel shank inserted into an equally soft medium*

Independent of their geometry and monomer concentration, the shanks were found to buckle *in vivo*. Because the buckling of the shank leads to significant deformation of the surrounding tissue, it is important to understand the origins of the phenomenon and the mechanisms at play to determine when it might be avoided or mitigated by design. *In vivo,* the shanks were prevented from expanding along the implant axis by the silicone sealant and dental cement applied at the shanks' insertion point. Conversely, *ex vivo,* shanks were inserted into the explanted brain and allowed to expand freely during re-swelling as no skull nor sealants were present. We reproduced both conditions – longitudinally constrained and un-constrained expansion – *in vitro* (Fig. S7). Shanks of de-hydrated rPAAm (3% AAm) were inserted into two agarose gel cubes. In the un-constrained case, the hydrogel shank began to twist as it started absorbing water from the agarose, however after several minutes

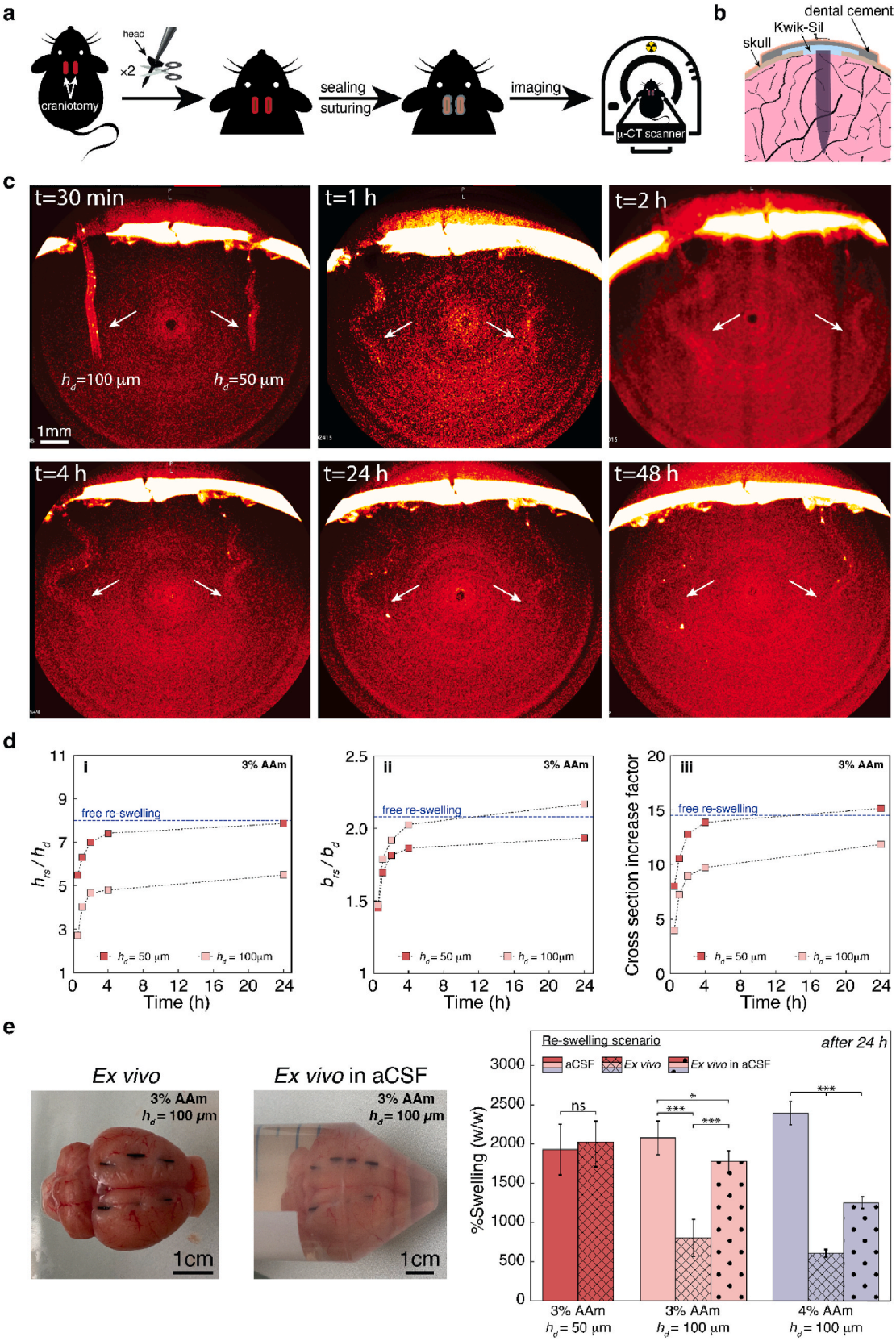

Fig. 3. Minimally invasive real time *in vivo* re-swelling study of rPAAm hydrogel shanks. a) Experimental approach for *in vivo* study of hydrogel shank re-swelling using micro-CT imaging. b) Schematic cross-section of the implanted rPAAm shank. c) 2-dimensional coronal slices of rPAAm shanks (3% AAm) implanted into rat brain at different time points post-implantation. Arrows indicate the shanks' positions inside the tissue. d) *In vivo* 1-D re-swelling curves of rPAAm shanks of different thicknesses. Thickness (*i*), width (*ii*) and cross-section (*iii*) relative increase curves. Values represent mean across 4 animals. e) Comparison of different re-swelling scenarios and the effect of shanks' initial dimensions (N = 6). * denotes $p < 0.05$, ** denotes $p < 0.01$ and *** denotes $p < 0.001$.

the twists straightened, and the shank appeared linear with a significant part protruding outside of the agarose gel cube as a result of longitudinal expansion associated with the re-swelling. In contrast, in the constrained case, achieved by securing a glass cover slip on the shank's insertion point, the hydrogel shank developed a twisted geometry, which amplified as the re-swelling progressed (Fig. 4a). The evolution of the buckling geometry, as characterized by the generation of the shank tortuosity and the increased buckling amplitude, could be visualized by overlaying the shank's centerline evolution over time as re-swelling progressed (Fig. 4b). The development of the buckled shank geometry followed a clear pattern of increasing amplitude without significant displacement of the shank's tip location, suggesting its failure to advance deeper into the agarose gel to accommodate the longitudinal expansion, which was measured to be approximately 60%.

In order to better understand the buckling phenomenon, we used a 2D finite-element simulation of the re-swelling shank embedded in a soft matrix, representative of the brain tissue. Buckling occurs asymmetrically, with centerline deviations concentrated at the upper half of the shank. To evaluate the swelling-induced stress leading to the shank's buckling, the relative critical load factor provided by the simulation was compared across different cases. The load factor was normalized by the value obtained for a reference set of shank parameters ($E = 1$ kPa; $l = 4$ mm; $h = 200$ μm). The simulation reveals that increasing the thickness of the shank leads to fewer and larger twists (from 3 to 2), consistent with the observations of the implanted shank obtained via micro-CT scans (Fig. 4c–i). This is also accompanied by an increase in the normalized critical buckling load. Increasing the length of the shank, on the other hand, results in the opposite effect, both increasing the number of observed twists and reducing the normalized critical buckling load (Fig. 4c–ii). Stiffening the shank leads to an increase of the twists' radius, as well as a considerable increase of the normalized critical buckling load (5 times increase when comparing 0.5 and 2 kPa shanks) (Fig. 4c–iii). These results suggest that to prevent or reduce re-swelling-associated buckling of de-hydrated hydrogel shanks, shorter, thicker, and stiffer implants should be used, as these require higher load factors to initiate the buckling phenomenon.

4. Discussion

4.1. A phenomenological model for implant buckling

A phenomenological model offers additional insights into the re-swelling-driven buckling. The essential features of the shank's conditions upon implantation can be readily accounted for with a mechanical model of the shank at steady state. Notably, a higher buckling mode with multiple wavelengths is predicted for a rod confined in a sufficiently stiff elastic domain, as noted in many prior studies, some of which also account for poro-elasticity effects that are relevant to the system considered here [48,49]. The schematics of the model and the most important system variables are depicted in Fig. 4d–i. The model is adapted from a calculation of a beam embedded in an elastic matrix and uses several assumptions about the boundary conditions that we explain here. These assumptions are primarily motivated by consistency with the experimental observations. First, the de-hydrated hydrogel shank is defined to be constrained from elongation along the longitudinal axis and is thus modelled as a pinned-pinned rod. Therefore, when it elongates upon re-swelling, it is subject to a compressive stress along its axis, leading to an elastically unstable configuration. We furthermore assume that the shank re-swells slowly compared with the insertion time of the implant. Indeed, if the shank were to re-swell rapidly, the loss of shank stiffness would negatively affect insertion, as the softened hydrogel would not advance deeper into the tissue. The surrounding tissue modifies the classical buckling analysis. Because the shank deviates from the insertion axis once buckled, it must deform the adjacent tissue. This deformation comes at a cost that penalizes the amplitude (A) of the buckled implant. Because of the penalty associated with larger A, the buckling mode number (N) increases, leading to a more sinuous implant axis, and a higher curvature energy associated with the buckling mode. Ultimately, this simple model predicts that the buckling mode depends on the relative stiffness of the re-swollen implant and the surrounding tissue (E_1 and E_2, respectively), the geometry of the implant (thickness h and length l), and the elongation of the implant along the implant axis. Relationships between the elastic energy of the shank, the elastic energy of the tissue and the selected buckling mode are provided in the supplementary material.

This simple model has some limitations. Indeed, the pinned-pinned rod boundary conditions may over-predict the buckling mode number. The true buckling mode number will be lower because of the symmetry of the elastic domain, which demands that the implant applies zero torque on the tissue at its distal end, breaking the symmetry of the problem along the implant's insertion axis. Nevertheless, the scaling analysis provided in the supplementary material offers guidelines for the design of implants that swell upon insertion into the tissue. We furthermore assume that the implant will swell to equilibrium with the chemical potential of the physiological fluid in the tissue [50]. This equilibrium state will depend on the salt concentration and the concentration of macromolecules and other chemical species in the extracellular fluid (ECF), thus causing the axial deformation to vary with the tissue type and chemical composition, highlighting the importance of the chemical environment in the development of such implants [51].

The guidelines for the implant geometry suggested by the analytical model include the dependence of the buckling mode on implant thickness - thinner implants will result in a larger buckling mode (N), leading to more tortuous deformation of the tissue, consistent with the finite element simulations (Fig. 4c–i). The analysis also shows that for a thinner implant, the buckling mode selection is weaker, as is readily apparent from the broad minimum of the total elastic energy curve (U_{tot}) shown in Fig. 4d–ii. The weak selectivity of the buckling mode implies that factors not accounted for in our model, such as the distal boundary condition and friction between the implant and the tissue, might influence the emerging buckling mode. Finally, our scaling analysis shows that as the shank thickness increases, the optimal buckling mode (N^*), which corresponds to the minimal energy of the coupled shank-tissue system, decreases, as shown in Fig. 4d–iii. Since the relative cost for deformation of the shank in comparison with the tissue strongly depends on the thickness of the shank, increasing shank thickness implies convergence on the classical Euler buckling limit.

Both the analytical model and the finite element simulation use fundamental principles of mechanics to predict the mode number of a constrained swelling-induced buckling hydrogel implant. The numerical-based simulations successfully predict the buckling mode, and both the analytical and numerical calculations identify its strong dependence on the implant's thickness, consistent with both *in vivo* and *in vitro* experimental observations. It should be noted, however, that as opposed to the finite element simulation, the analytical model shows that the buckling mode is less sensitive to the relative stiffness, or to the relative longitudinal extension upon swelling than it is to the thickness (see SI for details).

4.2. Implications on the design of hydrogel-based neural implants

The buckling of the hydrogel implant could strongly affect the performance of hybrid shanks that may embed a variety of thin electronic materials. The resulting bending strains could, for example, cause an important increase in the electrical resistance of metallic conducting traces. In extreme cases, deformations resulting from the buckling might even lead to mechanical failure of the traces by exceeding their critical failure strains, in case these are not carefully placed in the device neutral plane [52–54], or if swelling of the hydrogel is not perfectly uniform between both planes of the shank. Materials and components placed on the implant surface or exposed interconnects at electrode openings, on the other hand, could be subjected to permanent and significant bending

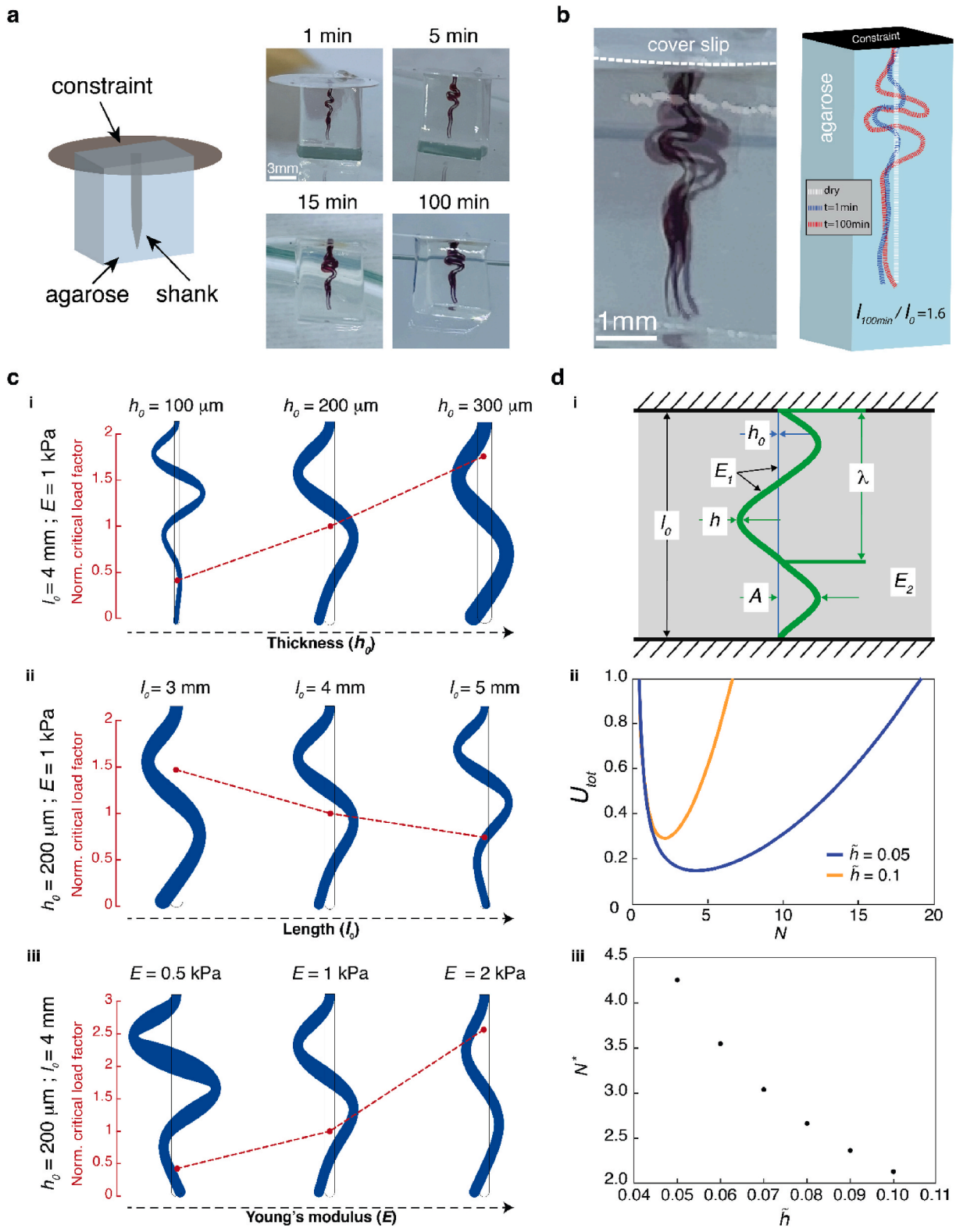

Fig. 4. Hydrogel shank buckling investigation. a) *In vitro* reconstruction of a de-hydrated hydrogel shank buckling inside a matrix. b) Overlay of hydrogel shank re-swelling in the constrained *in vitro* model at different time points. Photo overlays (left) and illustration of the shank's trajectory inside the agarose (right). c) Finite element model of laterally-constrained hydrogel shank buckling, varying the shank thickness h_0 (*i*), length l_0 (*ii*) and modulus E (*iii*). Trends of normalized critical load factor as function of simulation parameters (in red). d) Analytical model of swelling-initiated buckling of a hydrogel implant. (*i*) Schematics of initial (blue) a buckled (green) shank and main process parameters: l_o, h_o – initial length and thickness; h – buckled thickness; E_1, E_2 – shank and embedding matrix elastic modulus; A, λ – buckled geometry amplitude and wavelength. (*ii*) Dependence of the total energy of the coupled shank-tissue system (U_{tot}) on the buckling mode (N) for different normalized shank thicknesses ($\tilde{h}$). (*iii*) The optimal buckling mode (N^*) as a function of the normalized shank thickness ($\tilde{h}$). (For interpretation of the references to color in this figure legend, the reader is referred to the Web version of this article.)

strains (Fig. S8). For example, electrode coating materials typically used for neural recording and stimulation application are often based on brittle materials such as conducting polymers and metal oxides, which fail under tensile strains as low as several tenths of percent [55–58]. Hence, the use of the proposed analytical and computational tools, coupled with the developed *in vivo* imaging technique, could be used as potential design and validation tools for active soft hydrogel-based neural implants and aid in preventing or mitigating swelling-related outcomes.

5. Conclusions

The re-swelling process of a de-hydrated hydrogel is a complex and multi-faceted phenomenon that depends on a wide range of chemical, mechanical and thermodynamical parameters. When the re-swelling relies on water absorption from a biological tissue, additional considerations should be accounted for, such as the effects on the function of the implant. The initial hydrogel dimensions, tissue water content and its availability at the vicinity of the hydrogel, as well as implantation-related factors, have a substantial effect on the outcome of the re-swelling process, as we have shown here with a combination of experimental, numerical, and analytical tools and approaches. While the implants used in this work are purely hydrogel-based, and thus characterized by a higher mass and volume compared to the hydrogel components in functional neural interfaces, the same mechanisms should apply to the latter type and must be addressed when designing novel devices. Furthermore, hydrogels applied as coating layers are expected to be particularly prone to mechanical stresses and deformations during the re-swelling process due to the significant mechanical constraints arising from their immobilization on the devices' surface. Shear stresses can result in delamination of the hydrogel coating from the substrate and should be examined in relevant re-swelling scenarios. A low swelling ratio may be engineered in hydrogels at the expense of compliance.

The *in vivo* imaging technique developed in this work provides a powerful tool for the study of hydrogel implants inside soft tissues. The synthetic approach used to fabricate radiopaque hydrogels is highly versatile and can be easily adapted to other addition-type hydrogels used in various biomedical and tissue engineering applications, such as poly (2-hydroxyethyl methacrylate) (PHEMA), poly-N-isopropylacrylamide (pNIPAM), gelatin methacrylate (GelMA) and poly (sulfobetaine methacrylate) (PSBMA). Micro-CT based imaging of hydrogels can be used, for example, to track the distribution of hydrogel microspheres used for drug delivery applications, to analyze the conformability of hydrogel filling materials or to monitor the biodegradation of hydrogel scaffolds used for tissue regeneration. While the PAAm used in this study is an extreme case scenario in terms of its softness and high swelling ratio, it allowed the identification and amplification of the various factors and mechanisms, and their interplay during the re-swelling process. These should be therefore considered when developing the next generation of soft, hydrogel-based neural interfaces and examined systematically per each case to ensure the device performance after implantation and its compliance with the design specifications, in particular when relying on de-hydration and re-swelling steps as part of the delivery strategy. Furthermore, the proposed computational and analytical models can be utilized as design tools and provide important inputs for the development of reliable soft neural interfaces.

Credit author statement

M.S. and S.P.L. conceived the study. M.S. carried out the experiments and analysis. O.R. performed the surgeries. D.J.C and M.S. carried out the computed tomography. O.A. and J.M.K. conducted computational and analytical simulations. S.P.L. supervised the study and secured funding. M.S, O.A., J.M.K. and S.P.L. wrote the paper including edits from all authors.

Funding

This work was supported by Swiss National Science Foundation BSCGI0_157800 (SPL), the Bertarelli foundation (SPL), the European Union's Horizon 2020 research and innovation programme under the Marie Skłodowska-Curie grant agreement No. 754354 (OA).

Declaration of competing interest

The authors declare no competing interest.

Data availability

Data will be made available on request.

Acknowledgements

The authors thank Davide Demurtas (Interdisciplinary Centre for Electron Microscopy, EPFL, Lausanne, Switzerland) for assistance with transmission electron microscopy and Adele Fanelli (Medtronic Chair in Neuroengineering, EPFL, Geneva, Switzerland) for assistance with spectroscopic measurements.

Appendix A. Supplementary data

Supplementary data to this article can be found online at https://doi.org/10.1016/j.biomaterials.2023.122024.

References

[1] P. Fattahi, G. Yang, G. Kim, M.R. Abidian, A review of organic and inorganic biomaterials for neural interfaces, Adv. Mater. 26 (2014) 1846–1885.
[2] S.P. Lacour, G. Courtine, J. Guck, Materials and technologies for soft implantable neuroprostheses, Nat. Rev. Mater. 1 (2016), 16063.
[3] J.K. Nguyen, et al., Mechanically-compliant intracortical implants reduce the neuroinflammatory response, J. Neural. Eng. 11 (2014), 056014.
[4] S.M. Wellman, et al., A materials roadmap to functional neural interface design, Adv. Funct. Mater. 28 (2018), 1701269.
[5] X. Yang, et al., Bioinspired neuron-like electronics, Nat. Mater. 18 (2019) 510–517.
[6] A. Lecomte, E. Descamps, C. Bergaud, A review on mechanical considerations for chronically-implanted neural probes, J. Neural. Eng. 15 (2018), 031001.
[7] E. Musk, Neuralink, An integrated brain-machine interface platform with thousands of channels, J. Med. Internet Res. 21 (2019), e16194.
[8] F. He, R. Lycke, M. Ganji, C. Xie, L. Luan, Ultraflexible neural electrodes for long-lasting intracortical recording, iScience 23 (2020), 101387.
[9] B. Thielen, E. Meng, A comparison of insertion methods for surgical placement of penetrating neural interfaces, J. Neural. Eng. (2021), https://doi.org/10.1088/1741-2552/abf6f2.
[10] J. Liu, et al., Syringe-injectable electronics, Nat. Nanotechnol. 10 (2015) 629–636.
[11] Y. Liu, et al., Morphing electronics enable neuromodulation in growing tissue, Nat. Biotechnol. 38 (2020) 1031–1036.
[12] I.R. Minev*, et al., Biomaterials. Electronic dura mater for long-term multimodal neural interfaces, Science 347 (2015) 159–163.
[13] S. Budday, et al., Mechanical properties of gray and white matter brain tissue by indentation, J. Mech. Behav. Biomed. Mater. 46 (2015) 318–330.
[14] A. Goriely, et al., Mechanics of the brain: perspectives, challenges, and opportunities, Biomech. Model. Mechanobiol. 14 (2015) 931–965.
[15] S. Budday, T.C. Ovaert, G.A. Holzapfel, P. Steinmann, E. Kuhl, Fifty shades of brain: a review on the mechanical testing and modeling of brain tissue, Arch. Comput. Methods Eng. 27 (2020) 1187–1230.
[16] J.A. Chikar, J.L. Hendricks, S.M. Richardson-Burns, Y. Raphael, B.E. Pfingst, D. C. Martin, The use of a dual PEDOT and RGD-functionalized alginate hydrogel coating to provide sustained drug delivery and improved cochlear implant function, Biomaterials 33 (2012) 1982–1990.
[17] Y. Lu, et al., Poly(vinyl alcohol)/poly(acrylic acid) hydrogel coatings for improving electrode–neural tissue interface, Biomaterials 30 (2009) 4143–4151.
[18] K.C. Spencer, et al., Characterization of mechanically matched hydrogel coatings to improve the biocompatibility of neural implants, Sci. Rep. 7 (2017).
[19] Chen, A. et al. Zwitterionic polymer/polydopamine coating of electrode arrays reduces fibrosis and residual hearing loss after cochlear implantation. *Adv. Healthc. Mater.* n/a, 2200807.
[20] J. Goding, C. Vallejo-Giraldo, O. Syed, R. Green, Considerations for hydrogel applications to neural bioelectronics, J. Mater. Chem. B 7 (2019) 1625–1636.
[21] H.H. Barnett, et al., Poly (ethylene glycol) hydrogel scaffolds with multiscale porosity for culture of human adipose-derived stem cells, J. Biomater. Sci. Polym. Ed. 30 (2019) 895–918.

[22] Y. Liu, et al., Soft and elastic hydrogel-based microelectronics for localized low-voltage neuromodulation, Nat. Biomed. Eng. 3 (2019) 58–68.
[23] C.M. Tringides, et al., Viscoelastic surface electrode arrays to interface with viscoelastic tissues, Nat. Nanotechnol. 1 (2021) 11, https://doi.org/10.1038/s41565-021-00926-z.
[24] W.-C. Huang, et al., Ultracompliant hydrogel-based neural interfaces fabricated by aqueous-phase microtransfer printing, Adv. Funct. Mater. 28 (2018), 1801059.
[25] S. Oribe, et al., Hydrogel-based organic subdural electrode with high conformability to brain surface, Sci. Rep. 9 (2019), 13379.
[26] A. Sridharan, J.K. Nguyen, J.R. Capadona, J. Muthuswamy, Compliant intracortical implants reduce strains and strain rates in brain tissue *in vivo*, J. Neural. Eng. 12 (2015), 036002.
[27] D.-H. Kim, J.A. Wiler, D.J. Anderson, D.R. Kipke, D.C. Martin, Conducting polymers on hydrogel-coated neural electrode provide sensitive neural recordings in auditory cortex, Acta Biomater. 6 (2010) 57–62.
[28] S. Park, et al., Adaptive and multifunctional hydrogel hybrid probes for long-term sensing and modulation of neural activity, Nat. Commun. 12 (2021) 3435.
[29] P.T. Luong, M.B. Browning, R.S. Bixler, E. Cosgriff-Hernandez, Drying and storage effects on poly(ethylene glycol) hydrogel mechanical properties and bioactivity: drying and Storage Effects on Poly(Ethylene Glycol) Hydrogel, J. Biomed. Mater. Res. 102 (2014) 3066–3076.
[30] J.S. Temenoff, Emilys Steinbis, A.G. Mikos, Effect of drying history on swelling properties and cell attachment to oligo(poly(ethylene glycol) fumarate) hydrogels for guided tissue regeneration applications, J. Biomater. Sci. Polym. Ed. 14 (2003) 989–1004.
[31] S. Butylina, S. Geng, K. Oksman, Properties of as-prepared and freeze-dried hydrogels made from poly(vinyl alcohol) and cellulose nanocrystals using freeze-thaw technique, Eur. Polym. J. 81 (2016) 386–396.
[32] A.K. Denisin, B.L. Pruitt, Tuning the range of polyacrylamide gel stiffness for mechanobiology applications, ACS Appl. Mater. Interfaces 8 (2016) 21893–21902.
[33] T. Boudou, J. Ohayon, C. Picart, P. Tracqui, An extended relationship for the characterization of Young's modulus and Poisson's ratio of tunable polyacrylamide gels, Biorheology 43 (2006) 721–728.
[34] T. Takigawa, Y. Morino, K. Urayama, T. Masuda, Poisson's ratio of polyacrylamide (PAAm) gels, Polym. Gels Netw. 4 (1996) 1–5.
[35] F.D. Martinez-Garcia, et al., A beginner's guide to the characterization of hydrogel microarchitecture for cellular applications, Gels 8 (2022) 535.
[36] R. Aston, K. Sewell, T. Klein, G. Lawrie, L. Grøndahl, Evaluation of the impact of freezing preparation techniques on the characterisation of alginate hydrogels by cryo-SEM, Eur. Polym. J. 82 (2016) 1–15.
[37] Z. Kaberova, et al., Microscopic structure of swollen hydrogels by scanning electron and light microscopies: artifacts and reality, Polymers 12 (2020) 578.
[38] J. Ricka, T. Tanaka, Swelling of ionic gels: quantitative performance of the Donnan theory, Macromolecules 17 (1984) 2916–2921.
[39] N. Žuržul, et al., Donnan contribution and specific ion effects in swelling of cationic hydrogels are additive: combined high-resolution experiments and finite element modeling, Gels 6 (2020) 31.
[40] J. Weickenmeier, et al., Brain stiffens post mortem, J. Mech. Behav. Biomed. Mater. 84 (2018) 88–98.
[41] C. Wang, N.T. Flynn, R. Langer, Controlled structure and properties of thermoresponsive nanoparticle–hydrogel composites, Adv. Mater. 16 (2004) 1074–1079.
[42] L.E. Cole, R.D. Ross, J.M. Tilley, T. Vargo-Gogola, R.K. Roeder, Gold nanoparticles as contrast agents in x-ray imaging and computed tomography, Nanomed 10 (2015) 321–341.
[43] Y.C. Dong, et al., Effect of gold nanoparticle size on their properties as contrast agents for computed tomography, Sci. Rep. 9 (2019).
[44] V. Baudrie, J. Roullet, Y. Goureau, F. Chaouloff, J. Elghozi, Determination of cerebrospinal fluid production rate using a push-pull perfusion procedure in the conscious rat, Fundam. Clin. Pharmacol. 4 (1990) 269–274.
[45] J.K. Karimy, et al., A novel method to study cerebrospinal fluid dynamics in rats, J. Neurosci. Methods 241 (2015) 78–84.
[46] J.P. Harris, et al., Mechanically adaptive intracortical implants improve the proximity of neuronal cell bodies, J. Neural. Eng. 8 (2011), 066011.
[47] G.Y. Yang, Y.-H. Wen, C. Foldy, W.C. Tang, I. Soltesz, Sensor for stiffness measurements within the adult rat Hippocampus, IEEE Sensor. J. 8 (2008) 1894–1899.
[48] Y. Li, N. Kaynia, S. Rudykh, M.C. Boyce, Wrinkling of interfacial layers in stratified composites: wrinkling of interfacial layers, Adv. Eng. Mater. (2013), https://doi.org/10.1002/adem.201200387 n/a-n/a.
[49] J.M. Skotheim, L. Mahadevan, Dynamics of poroelastic filaments, Proc. R. Soc. Lond. Ser. Math. Phys. Eng. Sci. 460 (2004) 1995–2020.
[50] S.A. Chester, L. Anand, A coupled theory of fluid permeation and large deformations for elastomeric materials, J. Mech. Phys. Solid. 58 (2010) 1879–1906.
[51] W. Hong, X. Zhao, J. Zhou, Z. Suo, A theory of coupled diffusion and large deformation in polymeric gels, J. Mech. Phys. Solid. 56 (2008) 1779–1793.
[52] Z. Suo, E.Y. Ma, H. Gleskova, S. Wagner, Mechanics of rollable and foldable film-on-foil electronics, Appl. Phys. Lett. 74 (1999) 1177–1179.
[53] F. Fallegger, et al., MRI-Compatible and conformal electrocorticography grids for translational research, Adv. Sci. (2021), 2003761, https://doi.org/10.1002/advs.202003761.
[54] M. Vomero, et al., Conformable polyimide-based μECoGs: bringing the electrodes closer to the signal source, Biomaterials 255 (2020), 120178.
[55] P. Murray, G.M. Spinks, G.G. Wallace, R.P. Burford, In-situ mechanical properties of tosylate doped (pts) polypyrrole, Synth. Met. 84 (1997) 847–848.
[56] R.A. Green, N.H. Lovell, G.G. Wallace, L.A. Poole-Warren, Conducting polymers for neural interfaces: challenges in developing an effective long-term implant, Biomaterials 29 (2008) 3393–3399.
[57] U. Lang, N. Naujoks, J. Dual, Mechanical characterization of PEDOT:PSS thin films, Synth. Met. 159 (2009) 473–479.
[58] M.D. Ferro, N.A. Melosh, Electronic and ionic materials for neurointerfaces, Adv. Funct. Mater. 28 (2018), 1704335.